Microstructures and mechanical properties of reduced activation ferritic/martensitic steel fabricated by laser melting deposition

Junyi Feng[a,b], Peilei Zhang[a,b,c,*], Zhiyuan Jia[a,b], Zhishui Yu[a,b,*], Chao Fang[d,*], Hua Yan[a,b], Haichuan Shi[a,b], Yingtao Tian[e]

[a]School of Materials Engineering, Shanghai University of Engineering Science, Shanghai 201620, China

[b]Shanghai Collaborative Innovation Center of Laser of Manufacturing Technology, Shanghai 201620, China

[c]Fraunhofer Institute for Laser Technology ILT, Aachen 52074, Germany

[d]Institute of Plasma Physics, Chinese Academy of Sciences, Hefei 230031, China

[e]Department of Engineering, Lancaster University, Lancaster LA1 4YW, United Kingdom

ABSTRACT

Laser melting deposition (LMD) is a promising way for the fabrication of complex reduced activation ferritic/martensitic (RAFM) steel components which provides an exceptional opportunity to improve the existing designs and move toward fabricating fine features and complex geometries with higher efficiencies. It is well known that if steel members are welded together, defects will be concentrated in the welded joint. We can control the scanning path of the laser to achieve a complex component molding, avoiding welding. Considering the LMD technology, the results of each layer of powder molding will affect the fineness of the final processed products, such as laser power, scanning speed, defocus and so on, which are all important factors affecting the products. We control the size of powder particle size as a variable to conduct a study on RAFM steel supplemented by LMD technology for the first time, and its microstructure and grain size were analyzed. In terms of mechanical properties, its hardness, Charpy impact, tensile strength and elongation were measured. The results show that compared with other processing processes including Selective Laser Melting (SLM), rolling, welding joints, the tensile strength of RAFM steel manufactured by laser coaxial powder feeding is up to 1057.75 MPa, and there are no pores and almost no defects when using small particle size powder. The microstructure of LMD RAFM steel contains a large amount of lath martensite and δ-ferrite, and some precipitates such as Mx, whose average grain size decreases with the increase of powder particle size (5-150 μm). In this study, the laser additive process was monitored by high-speed photography, and the average grain size of LMD RAFM steel was further analyzed, and a reasonable explanation of its mechanical properties was given.

---

[*] Corresponding authors: Peilei Zhang (peilei@sues.edu.cn) , Zhishui Yu (yu_zhishui@163.com) and Chao Fang (fangchao@ipp.ac.cn)

Introduction

Due to the abundant fuel resources, strong operability, zero carbon emission and low operating cost of nuclear fusion power generation, the feasibility of nuclear fusion power generation has attracted extensive attention [1–6]. Reduced Activation Ferritic/Martensitic(RAFM) steels are selected as the main structure of candidate materials due to their excellent thermo physics, excellent irradiation-resistance, anti-expansion and good mechanical properties [7, 8]. Reduced activation ferritic/martensitic (RAFM) steel has been selected by International Thermonuclear Experimental Reactor (ITER) and China Fusion Engineering Test Reactor (CFETR) as the main candidate structural material for Test Blanket Module (TBM) [9–13].

The welding of RAFM steel is an inevitable link in industrial production. Careful control of welding parameters, such as preheating, welding temperature and post-weld heat treatment is the key to good welding quality. In the process of high or low stress creep loading, the weld strength is generally lower than the base metal, and weld or heat affected zone (HAZ) fracture occurs. For example, under the testing conditions of 600 ℃ and 100 MPa, the creep endurance life of the RAFM steel welded joint is 4271 h, which is much smaller than the 15740 h of the base metal when Type IV cracks in the HAZ [14, 15]. In addition to the problem of weak welding joints, complex geometries are also difficult to solve with a single welding technique.

With the wide application of nuclear energy, reduced activation ferritic/martensitic RAFM steel components tend to be complicated and refined, and components are increasingly strict in terms of material, structure and other aspects. Laser Additive Manufacturing (LAM) is widely used in aerospace, automotive manufacturing, bio-medical, energy and power fields because of its high flexibility, high material utilization and other characteristics. At present, according to the powder transportation mode LAM two typical stable forming processes have been formed [16–18]. One is Laser Melting Deposition (LMD) based on synchronous powder feeding, which is mainly used for rapid prototyping of large and complex components. However, the dimensional accuracy of components is not high, and post-processing is required to achieve application requirements [19–21]. The other is based on Selective Laser Melting (SLM) for Powder Paving, due to its high forming accuracy, but the processing size of the parts is limited, it is mainly used for direct precision forming of small or medium-sized complex components. B. Huang et al fabricated composite RAFM steel components using SLM and conducted a series of mechanical property tests and microstructure analysis on the samples [22, 23]. It is concluded that the anisotropy of microstructure is related to the differences in mechanical properties of the materials.

Theoretically, the presence of fine particles will be beneficial, as this would lead to an increase in the powders density which would reduce the number of defects in the printed parts and improve the surface roughness [24]. It is also known that smaller particle sizes have increased laser energy absorption, thus improving their processing. The advantages obtained by fine particles are contradicted by the significant disadvantages associated with their use, such as their high tendency to agglomerate[25], and their large surface area to mass ratio. Due to the irregular shapes and variable sizes of the agglomerates formed, fine powder agglomerates are more likely to promote the formation of pores and voids during processing. Therefore, we also adopted the parameter of powder particle size change in this experiment to observe the influence of powder particle size change on reduced activation ferrite/martensite RAFM steel.

In this study, we used laser coaxial powder feeding technology to fabricate composite reduced activation ferrite/martensite steel with different size of powder. The microstructure and the mechanical properties of the as-built samples was investigated with optical microscope (OM), scanning electron microscope (SEM) combined with the X-ray diffraction (XRD), electron back-scattered diffraction (EBSD) techniques, microhardness, impact fracture characterization and the tensile properties, were carried out to study the influence of different powder particle.

2. Experimental procedures

2.1 Materials

The 316L stainless steel was used as the substrate material with a thickness of 20 mm. The chemical composition of reduced activation ferrite/martensitic steel powder are shown in Table 1. The reduced activation ferrite/martensitic steel powders with different particle sizes (<25 μm, 15~53 μm, 45~105 μm, >100 μm) were selected for Laser melting deposition. To fabricate the RAFM steel with good performance, powders with excellent flowing were required. Meanwhile, the materials adopted in the experiment were RAFM powders, which were fabricated by the method of atomization comminuting process with RAFM steel. The micromorphology and XRD results of powders are shown in Fig.1, the powder has good sphericity. On considering the particle morphology, it can be seen that even coarse powders C and D consisted of highly spherical with a large number of satellite particles were also present. However, similar satellite particles were also seen in the thinnest powder (<25 μm).

Table 1 Chemical composition(wt%) of powders

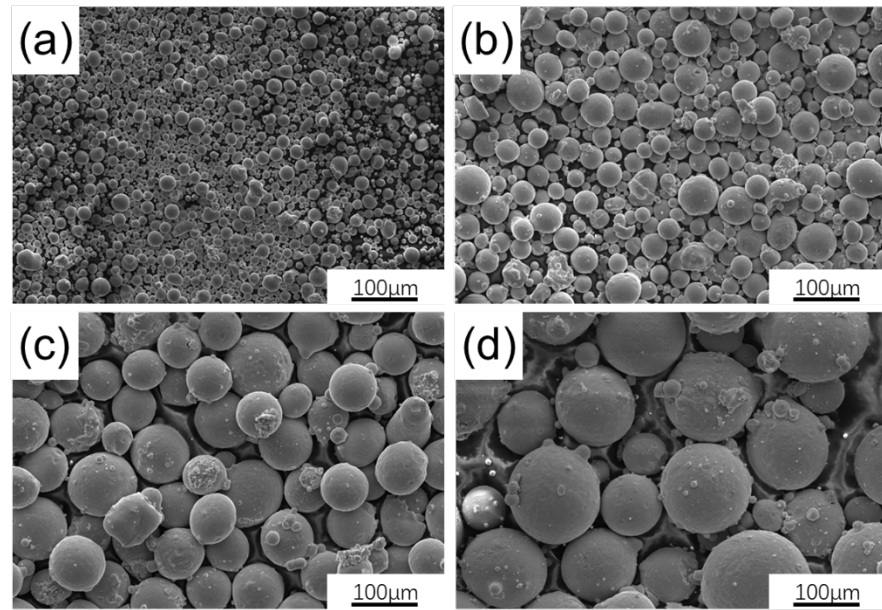| Element	Fe	Cr	Ta	V	W	Si	Mn	C
Content	Bal.	8.9	0.14	0.20	1.5	0.05	0.49	0.092

Fig.1. SEM images of different particle powder, (a) <25 μm, (b) 15~53 μm, (c) 45~105 μm, (d) >100 μm

2.2 Experimental equipment and methods

Coaxial powder feeding technology was applied in this study, the used coaxial powder feeding system is shown in Fig.2. The laser power was 2700 W and the welding speed was about 10 mm/s. The parameters of the coaxial powder feeder include the feeding speed of 5 rad/min, the flow rate of the powder carrier of 20 L/min and the flow rate of the protective gas of 40 L/min. The size of four fabrication samples for each powder particle size is 140 mm lengths, 40 mm widths and 15 mm heights. All the samples were prepared using the same scanning strategy as described above.

After the laser fabrication, fabrication samples are shown in Fig.3. We cut it off the substrate using a wire cutting method to make samples for a series of subsequent analyses. Metallographic samples were cut perpendicular to the scanning direction. The samples were grinded on emery papers and polished, then etched in Villella's reagent for 35 s. Optical microscope (OM), scanning electron microscope (SEM), electron back-scattered diffraction (EBSD) and X-ray diffraction (XRD) were used to analyze microstructure, element distribution and phases in the scanning direction. At the same time, in order to further study the additive manufacturing process, different particle size powder under the laser heat into the molten pool changes, we used high-speed photography to monitor the manufacturing process. Vicker's micro-hardness was measured by HX-1000TM/LCD at the fabrication zone from top to substrate on depth direction of every laser track with a load of 300 g and a holding time of 10 s. Fig.4 shows the production standards of impact samples and tensile samples. Tensile samples are made according to American standards ASTM-E8-16a.Tensile strength was evaluated on CMT5150 Universal tester with a constant

displacement rate of 1mm/min. Charpy impact test sample is made according to GB/T229-2007, the size of 55 lengths, 10 widths and 10 heights which is v-notch (the notch depth is 2 mm, the included Angle is 45°and the curvature radius at the bottom is 0.25 mm). Impact test equipment for the drop hammer impact testing machine, model for INSTRON9350. Fig.5 shows Charpy impact sample, tensile sample and tensile specimen produced in this experiment.
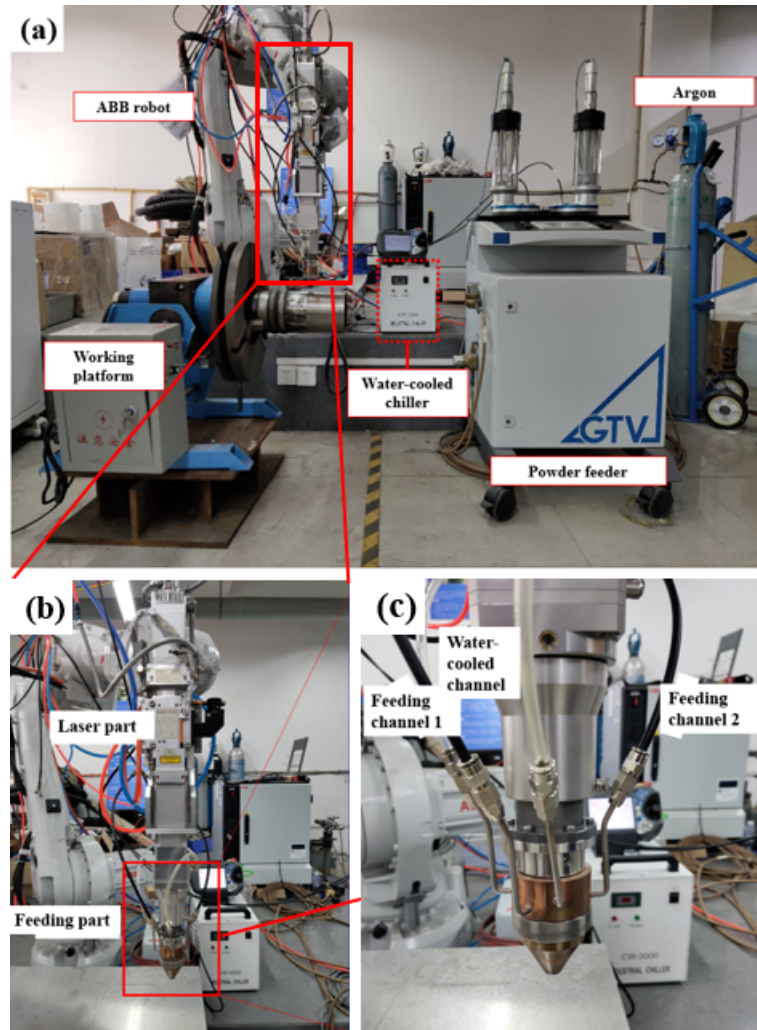

Fig.2. Coaxial feeding system, including ABB robot and feeding machine: (a) Operation system, (b) Laser coaxial powder feeding head, (c) Cladding head parts
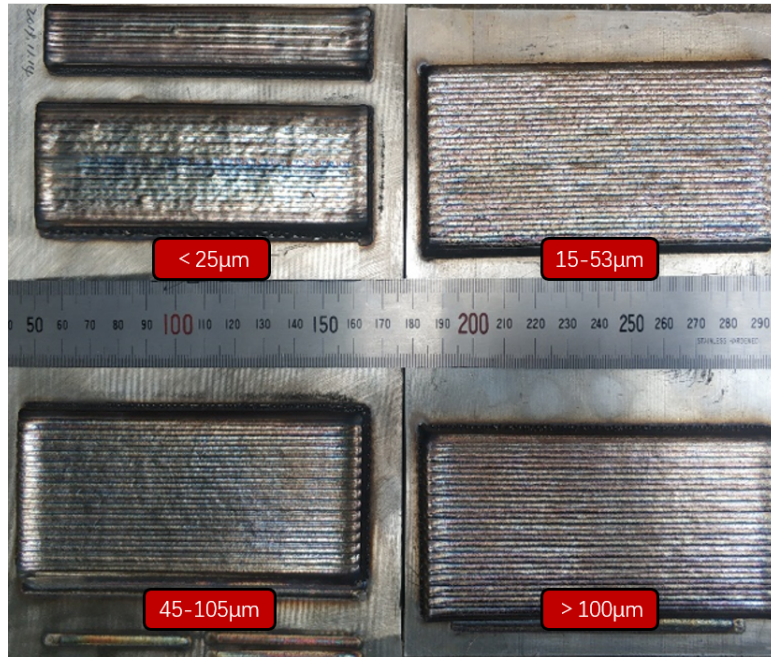
Fig.3. Sample of RAFM steel with different powder particle manufactured by laser additive manufacturing
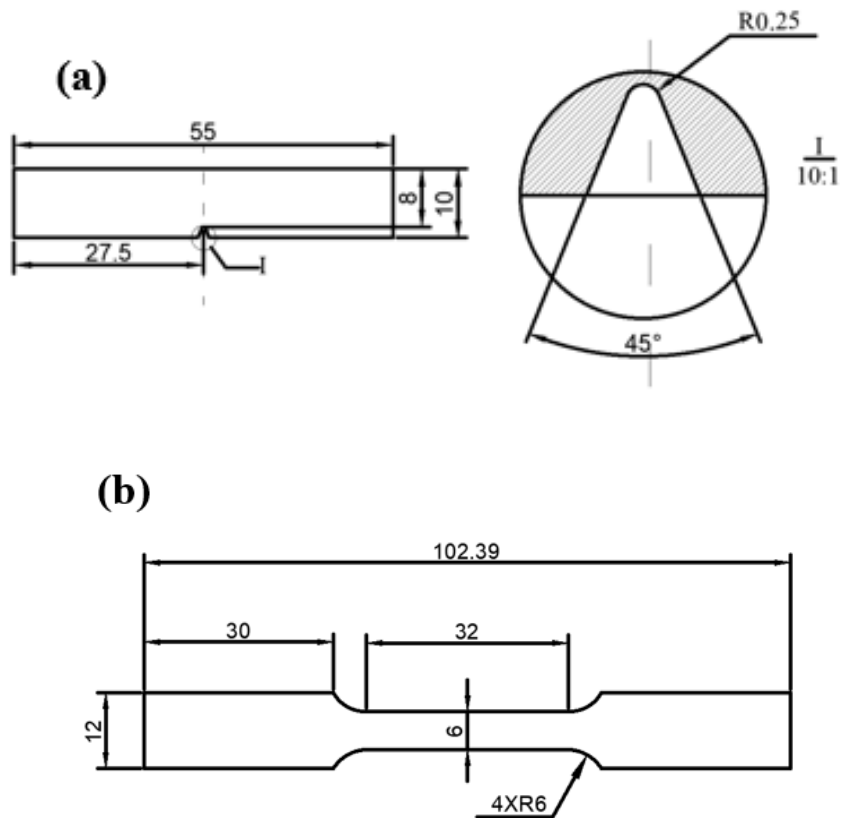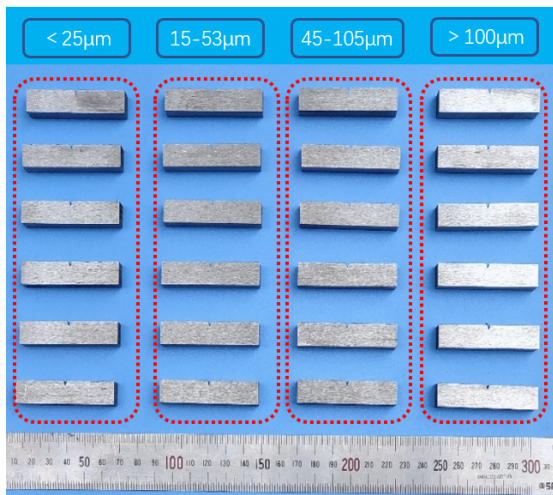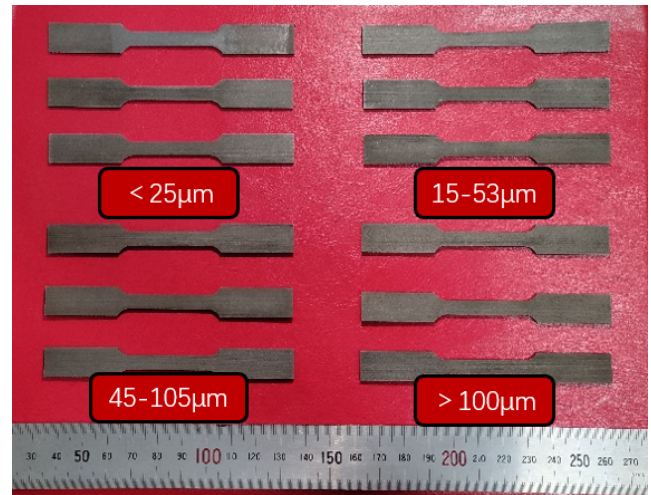

Fig.4 (a) Standard for Charpy impact specimens is GB/T229-2007, (b) Standard for tensile specimens is

ASTM-E8-16a

(a)   (b)

Fig.5 (a) Charpy impact test sample (b) Tensile test sample

3. Results and discussion

3.1 Microstructural Characterization

The cross-section of all samples perpendicular to the scanning direction were first observed using OM, and the results are shown in Fig.6. It can be seen that RAFM steel with particle size less than 25 μm has obvious unfused parts from Fig.6(a). The particle size of the powder is too small, easy to bond, and the clusters seriously reduce the fluidity of the powder. In addition, due to the small particle size and single distribution of RAFM steel, its bulk density and vibration density are small, and the laser powder cannot be scanned uniformly, which results in the parts not being fused [26]. Moreover, during the forming process, the phenomenon of powder rebound and splashing with large particle size is serious, and the molten pool that actually enters the alloy powder is very small, so the utilization rate of the powder is very low.

Fig.6(b) and Fig6(c) show the metallographic pattern of RAFM steel with powder particle sizes ranging from 15~53 μm and 45~105 μm. After corrosion, each layer can be clearly seen to be completely fused with each other, but there are a few pores appeared in the samples made of powder particle size 45-105 μm, which are caused by the increase of powder particle size and the increase of space between the powders, some gas was solidified in the molten pool before it could escape. Fig.6(d) shows that the particle size of the powder is above 100 μm. Although the fluidity is the best, there is a large gap between the large powder particles, which is easy to form pores in the forming process, and the number of pores is significantly increased. The gas source mainly has two aspects: on the one hand, the alloy powder itself has too high gas element content, and the solubility is reduced during the rapid cooling of the molten pool and the solidification process, and the precipitated gas cannot be eliminated in time; After the gas enters the solution pool, if the gas escape speed is greater than the solidification speed of the gold

bending in the solution pool, the pore defects will not form inside the forming part. On the contrary, if the stomatal defects are too late to escape, they will remain in the tissue and form the stomatal defects. We chose a powder with a low gas element content, which can eliminate the first influence factor, and we used high-speed photography to further explore the reason for the increased porosity. In order to further study the change of powder particle size entering the molten pool under laser heat during additive manufacturing process, we used high-speed photography to monitor the manufacturing process as Fig.7 shows. When a laser beam is focused on the RAFM steel, a melt pool is formed under the laser focusing spot and as the laser beam is moved away during scanning a rapid solidification process takes place inside each melt pool immediately. We monitored the LMD construction process of fine powder and coarse powder with high-speed photography[27]. We set a reference line on the substrate, from the laser scan to the start of the reference line, recorded as time 0 ms. During the process of high-speed photography of 15-53 μm powder laser additive, the image was saved at an interval of 150 ms. The total time from the beginning of the laser crossing the reference line to the complete solidification of the region on the reference line was 706 ms. The > 100 μm powder laser additive was captured by high-speed photography at an interval of 100 ms. The time from the beginning of the laser crossing the reference line to the complete solidification of the area on the reference line was 418 ms. In addition to the comparison of time, the shape of the molten pool is also compared. We measured the length of the molten pool in the process of 15-53 μm powder laser additive according to the scale, and the length of the molten pool is only 6.89 mm in the process of > 100 μm powder laser additive while the length of the molten pool is 10.87 mm in the process of 15-53 μm powder laser additive much longer. Obviously, it can be seen that the length of the molten pool in the coarse powder is smaller than that in the fine powder and the solidification time of coarse powder laser additive is far less than that of fine powder, which means that the solidification rate of the molten pool in the additive manufacturing of coarse powder is faster than that of the fine powder. The results show that the melting pool solidification rate of RAFM steel large-size powder is faster in the process of LMD, and the gas brought into the molten pool by the powder will have less time to escape from the molten pool. Compared with small-size powder, more gas brought into the molten pool can't escape before the solidification of the molten pool, resulting in more pores in the prepared sample. When powders with different particle sizes are added by laser, the solidification rate of molten pool will have a significant influence on the grain growth and mechanical properties later, which will be mentioned later

There's another thing that we can get from high-speed photography image, according to the Fig.7(c) diagram of different particle size powder feeding focusing, powder gathering focal length with the decrease of the powder particle size has a tendency to increase. This is because the smaller the particle size of the powder, the smaller the

corresponding inertia, and the greater the influence of the air flow filed distribution, the position where it becomes a cone-shaped blast air area will be lower, therefore, it will converge to focus.
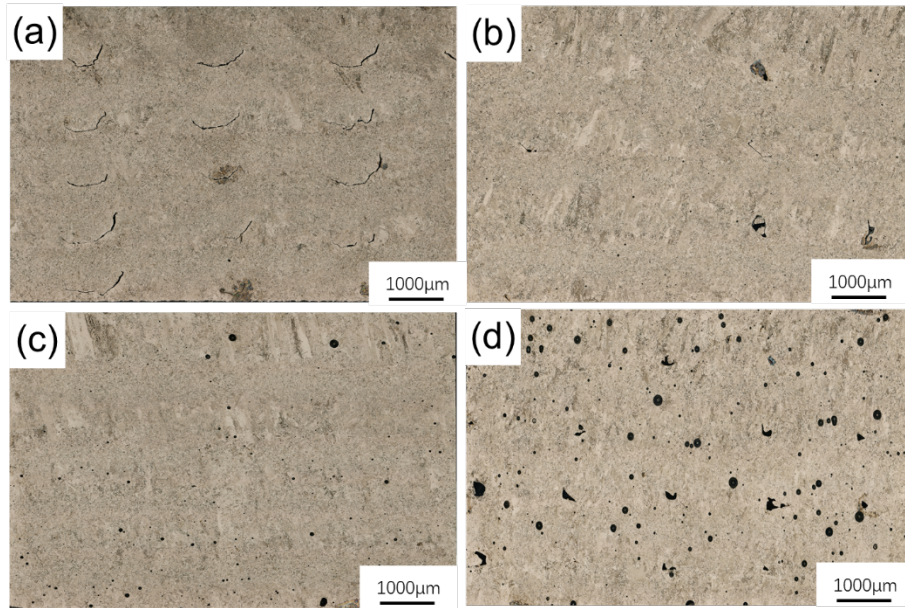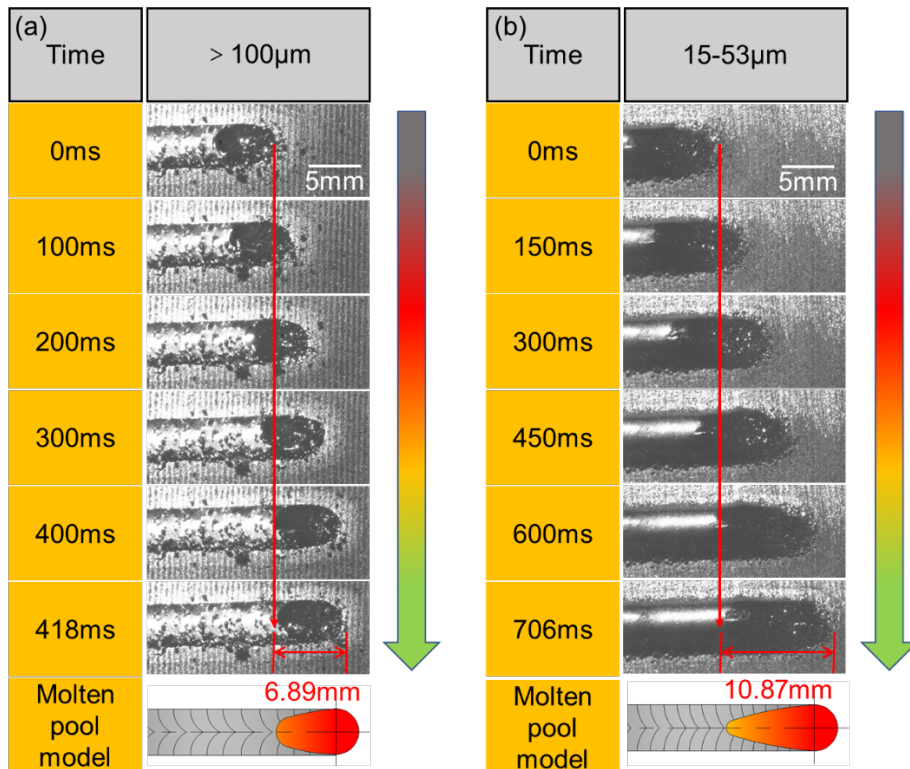

Fig. 6. Macroscopic metallography of RAFM steel with different powder particle size by laser additive manufacturing, (a) <25 μm, (b) 15-53 μm, (c) 45-105 μm, (d) >100 μm
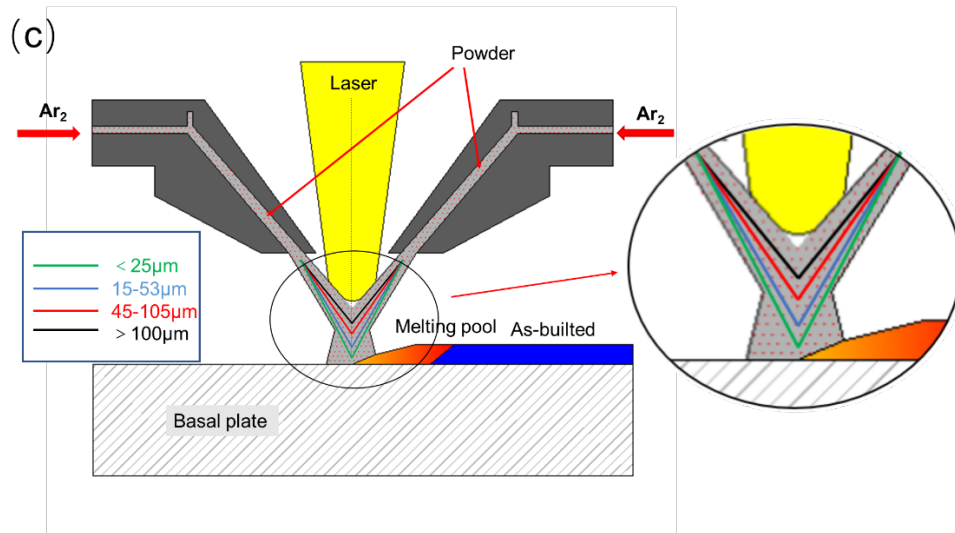
Fig. 7 Images from high-speed photography (a) >100 μm top view of molten, (b) 15-53 μm top view of molten, (c) diagram of different particle size powder feeding focusing

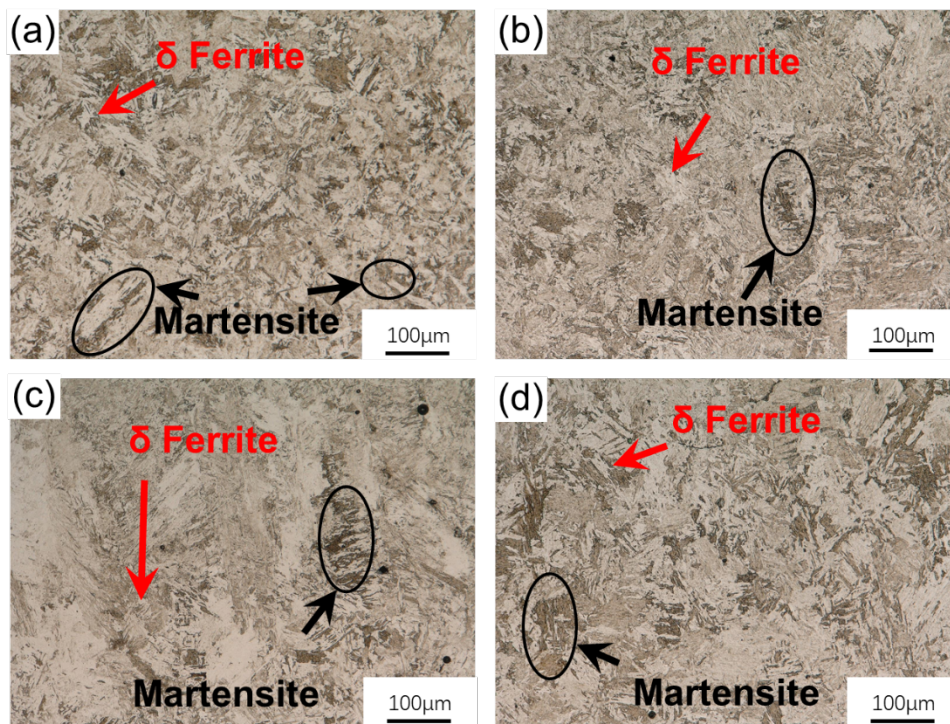

Fig. 8. Microscopic metallography of RAFM steel with different powder particle size by laser additive manufacturing, (a) <25 μm, (b) 15-53 μm, (c) 45-105 μm, (d) >100 μm

Fig.8 shows the microstructure of RAFM steel with different powder particle size augmentations. In the whole microscopic metallographic image, δ-ferrite and martensite with different orientations are dominant. The light-colored area is δ-ferrite, while the uneven black area is mostly lath martensite, and part of it is other precipitated phases under the influence of secondary heat. This indicates that the microstructure of the alloy is mainly composed

of δ-ferrite and fine lath martensite. Layered martensite of similar size and uniform distribution can be observed in the microstructure of four different particle size reduction activated martensitic stainless steels. Compared with austenitic stainless steel, martensitic steel has stronger resistance to radiation helium embrittlement and radiation swelling ability, which is due to its volumetric cubic structure. Comparing various RAFM steel at home and abroad, it is found that the content of alloying elements is slightly different, and the preparation method and subsequent heat treatment process are similar. The basic structure is ferrite and martensite, and the precipitated phase contains a large amount of carbide. In terms of grain boundaries and precipitation, $M_{23}C_6$ has two deposition types (where M is mainly for the Fe, Cr) and MX type (TaC, TaN, VC, VN). The XRD patterns of the four kinds of particle size powder manufacturing RAFM steel are shown in Fig.9. After removing the miscellany peak, it can be clearly seen that the peak of a-Fe/Cr is in the XRD image. Generally, $M_{23}C_6$ carbides rich in chromium and MX carbonitrides rich in vanadium and tantalum are two precipitates which contribute to the dispersion strengthening of RAFM steel. MX carbonitride is much finer than $M_{23}C_6$ carbide and is mainly distributed in the lath, while $M_{23}C_6$ carbide precipitates along the lath, block, packet and prior austenite grain boundaries.[28]

Fig.10 and Table 2 shows the scanning area and composition results of energy spectrum of RAFM steel prepared by laser-additive manufacturing. It can be seen that the element composition of RAFM steel prepared by coaxial powder feeding laser-additive is similar to that of common RAFM steel elements. There is no obvious segregation occurred during the additive process. This indicates that the powder particle has no effect on the microstructure of RAFM steel manufactured by laser-additive.
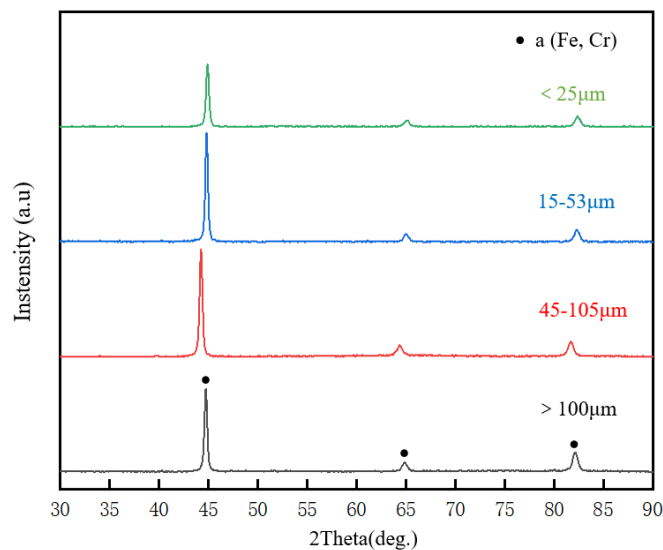

Fig.9. XRD patterns of the four kinds of particle size powder manufacturing RAFM steel
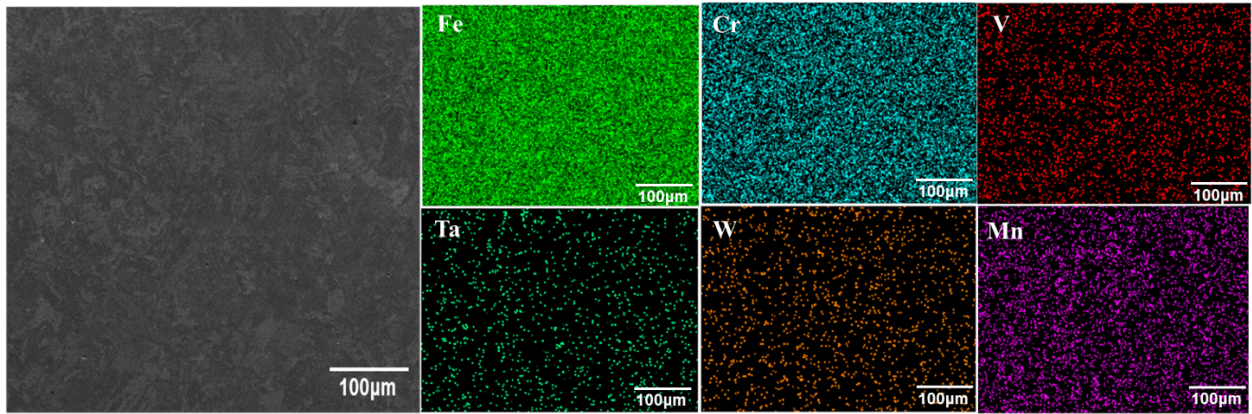
Fig. 10. Laser melting deposition RAFM steel (≤25 μm) energy spectrum scanning, (a)region, (b) element

distribution

Table 2 The results of energy spectrum scanning composition of RAFM steel (≤25 μm) prepared by laser

melting deposition (wt%)

Element	Fe	Cr	C	W	V	Ta	Mn	O
Content	85.9	8.9	2.8	1.3	0.3	0.15	0.35	0.3

3.2 Effect of grain orientation and grain size

The influence of grain size and width of martensite lath on performance is mainly related to the grain boundary or lath grain boundary, which is manifested as hindering the movement of dislocations at the grain boundary or lath boundaries that hinder the movement of dislocations and between grain boundaries and grain boundaries interaction. Fig.11 is the EBSD Inverse Pole Figure (IPF) of RAFM steel with different particle sizes, reflecting the grain orientation in the material. In the upper right corner of each figure, the illustration is an oriented triangle, in which different colors represent different grain orientations, red represents grains parallel to the surface orientation [111] of the sample, blue represents grains parallel to the surface orientation [001] of the sample, and green represents grains parallel to the surface orientation [101] of the sample. The IPF distribution diagram was disorganized in color, with uniform grain distribution and no obvious texture. At the same time, many parallel martensitic slats can be seen in the plate block. Martensitic slats are relatively thick and long, and the orientation of martensitic slats is randomly distributed. In the EBSD image, powders with different particle sizes were further coated with laser additive. Their structures were almost the same, and particle sizes had little influence on the construction of the sample

The grain size is also an important factor affecting the mechanical properties of RAFM steel. Fig.12 shows the

grain size distribution of four kinds of particle size powder after additive. The results show that the average grain size of the powder additive less than 25 μm reaches the maximum of 3.171 μm. The average grain size of the as-built decreases gradually with the increase of the particle size （10-150 μm）of the powder used in laser manufacturing. The average grain size of the powder additive > 100 μm reaches the minimum of 2.054 μm. This is mainly because the above analysis concluded that the larger the particle size of the powder, the faster the solidification rate of the molten pool. The faster the solidification rate of the molten pool, the lower the actual crystallization temperature, the greater the degree of undercooling, the higher the nucleation rate, and thus the smaller the grain size. [29].

The laser melting temperature gradient (G_L), solidification undercooling (ΔT) and growth rate(R) in the molten pool are significantly different from one local area to another, the microstructure changes. The influence of the solute and thermal gradient described under cooling conditions on the solidification structure can be expressed mathematically by the following equation [29, 30].

$$\frac{G_L}{R} < \frac{\Delta T}{D_L} \text{ For plane equiaxed solidification} \tag{1}$$

$$\frac{G_L}{R} > \frac{\Delta T}{D_L} \text{ For cellular and columnar solidification} \tag{2}$$

Where, D_L is the diffusion coefficient.

The G_L/R ratio determines the stability of the solidified microstructure. Continuously expect plane, columnar and equiaxed dendritic structure from high to low ratios. While the G_L/R ratio controls the solidification microstructure, the cooling rate in terms of GL*R determines the fineness of the structure, the higher the product the finer the structure. According to EBSD images, columnar grains are the main grains formed in the structure which is typical for any fast solidification process.
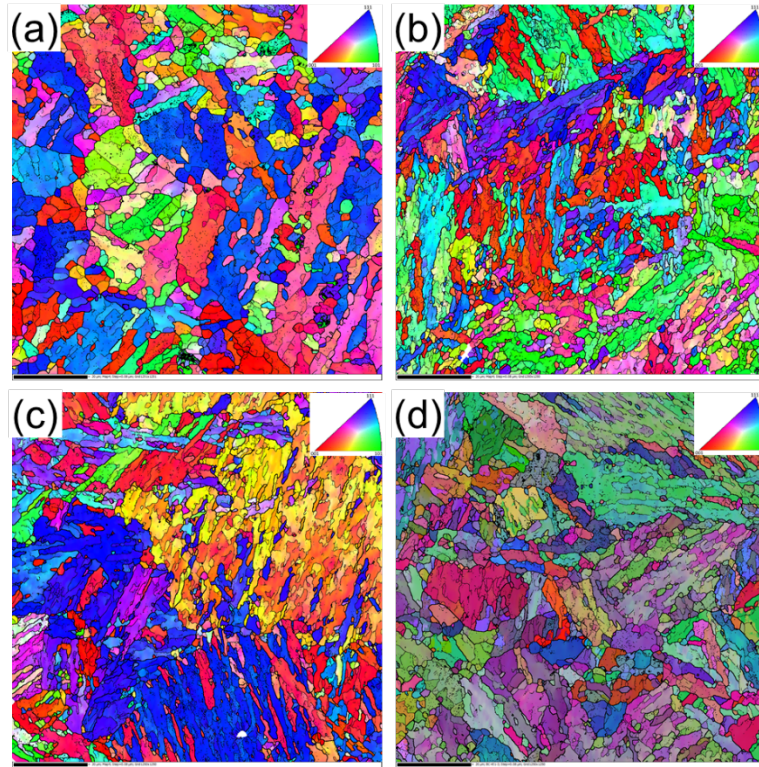
Fig. 11 IPF diagram of EBSD analysis of RAFM steel with different particle sizes, (a) ≤25 μm, (b) 15-53 μm, (c) 45-105 μm, (d) >100 μm
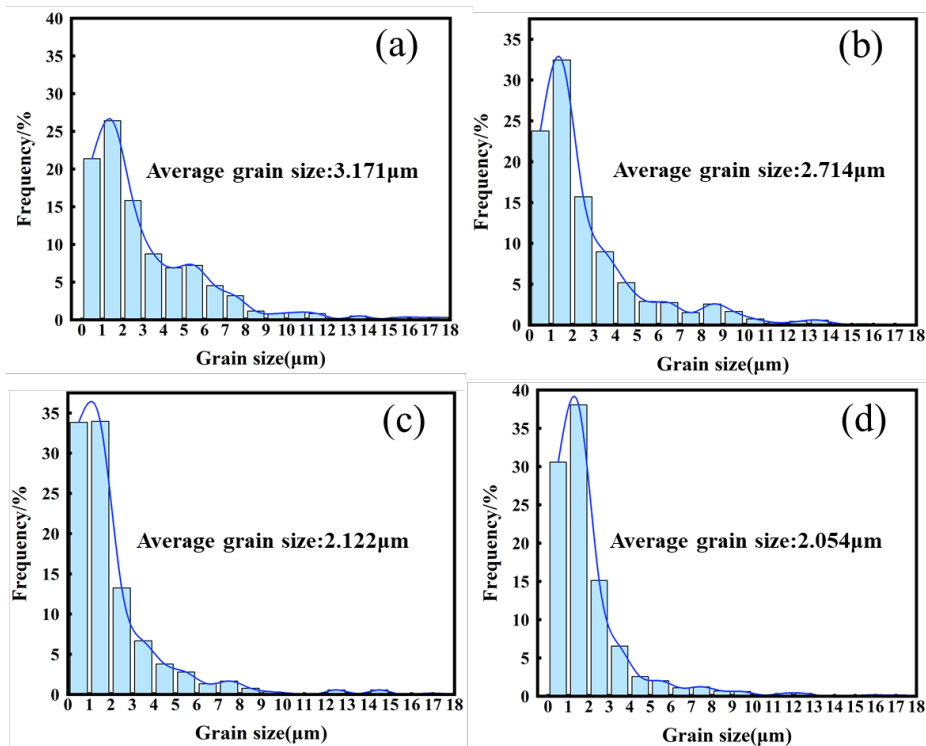

Fig. 12. Grain size distribution of RAFM steel with different powder particle sizes, (a) <25 μm, (b) 15-53 μm, (c) 45-105 μm, (d) >100 μm

3.3 Mechanical properties

3.3.1 Charpy impact property

Fig.13 shows the Charpy impact performance of RAFM steel with different powder particle size additive. Due to open a v-notch specimen under the impact load caused by stress concentration near the notch, it can be seen that the Charpy impact energy of RAFM steel with > 100 μm reaches the highest 15 J, it shows that the toughness is relatively good, this is mainly due to its small grain size. The Charpy impact energy is generally low, which indicates that RAFM steel prepared by LMD method has the disadvantages of insufficient toughness and stress concentration, and it needs to be toughened by subsequent heat treatment and other processes.
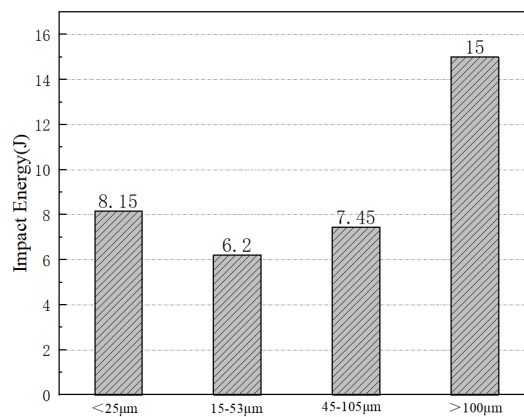

Fig. 13. Charpy impact energy of RAFM steel with different particle size powder laser-additive

3.3.2 Tensile property

The tensile test of RAFM steel with different particle size powder additive was carried out, and the test results were shown in Figure 14 and Table 3. As the particle size of the powder increases, the tensile strength of the sample increases to a certain extent. Compared to the ultimate tensile strength of the wrought CLAM, almost all of the LMD-RAFM specimens could achieve the ultimate tensile strength (UTS) > 650 MPa[31]. When the particle size reaches 45-105 μm, the tensile strength reaches a maximum of 1057.7MPa, elongation rate is 12% which is also the maximum among four samples. With rapid cooling rate, the microstructure of LMD built RAFM was fine lath martensite, and there were some sub-boundaries which might contribute to the high strength of as LMD built RAFM.

In order to find out the reason for the change of tensile strength, we observed the fracture morphology, as shown in Fig. 15. On the one hand, it can be found that when the powder particle size is small (<25 μm, 15-53 μm), tensile fracture without porosity, cracks and other defects, forming good. On the other hand, there were many pores exist in samples whose powder particle size is large (45-105 μm, >100 μm), especially the tensile fracture of the

maximum particle size powder laser-additive has a great porosity, and the maximum pore diameter can reach 40 μm. When the particle size of powder is small, the tensile dimples of the laser-additive RAFM steel are thin and shallow. With the increase of the powder particle size, the dimples of the fracture morphology gradually become larger and deeper. But due to the presence of pores, the tensile strength did not increase all the way. In conclusion, the main fracture mechanism is ductility fracture and the mean size of dimples is similar to that of cellular grains of the fabrication RAFM steel, which was found in the work of Zhang et al[32], [33].

When the densification rate reaches the highest level (≥98%), according to the grain boundary strengthening theory, the grain size becomes the most important factor affecting the tensile strength, because a large number of grain boundaries hinder the movement of dislocations [33]. Therefore, the high tensile strength obtained can be attributed to the small unit cell size (0.3 to 1.4 μm) of the porous dendrites, and unlike traditional strengthening methods (such as work hardening), traditional strengthening methods sacrifice ductility, which enhances the material strength at the sacrifice of ductility, LMD-fabricated RAFM steel is strengthened without losing ductility.
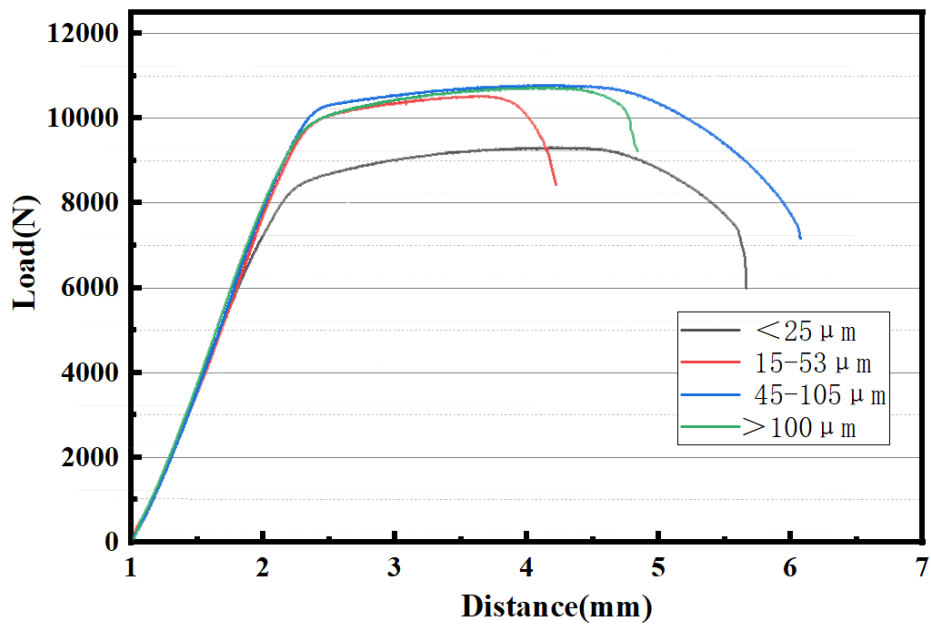

Fig. 14. Tensile curve of RAFM steel with different particle size powder laser-additive

Table 3. Tensile strength and elongation of RAFM steel with different particle size powder laser-additive

	<25 μm	15-53 μm	45-105 μm	>100 μm
Tensile Strength/MPa	926.77	1008.27	1057.75	1029.14

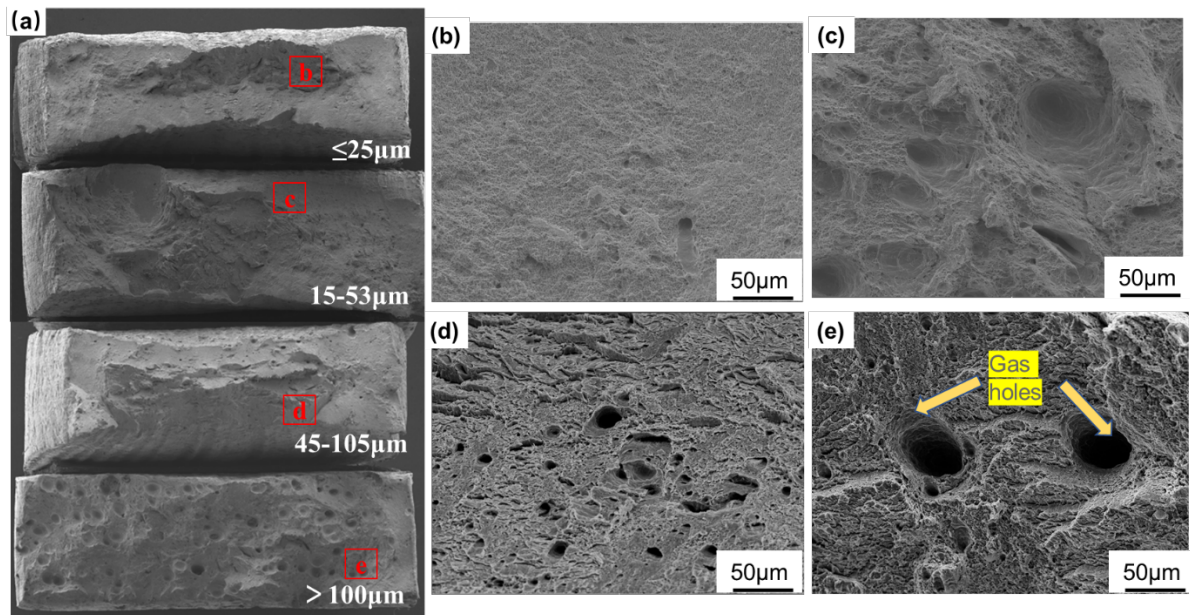|				
Elongation rate/%	8.60	9.10	12.00	8.90

Fig. 15. Laser-additive fabrication of RAFM steel tensile fractures with different particle powder, (a) <25 μm, (b) 15-53 μm, (c) 45-105 μm, (d) >100 μm

3.3.3 Microscopic Vickers hardness

The micro-Vickers hardness of RAFM with different particle size additive is shown in Fig. 16. The load imposed by the hardness test was 300 g, and the load holding time was 10 s. A hardness test point was made every 0.1 mm. The transverse (perpendicular to the weld) and longitudinal (parallel to the weld) hardness of the 4 samples were measured and the fluctuation of hardness was analyzed. According to the transverse and longitudinal comparative analysis, RAFM steel with 15-53 μm and 45-105 μm powder particle size additive has the highest hardness, which is due to the small average grain size of these two kinds of powder particle size, resulting in higher hardness. RAFM steel with > 100 μm particle size powder additive has many defects such as pores, which leads to great fluctuation of its hardness. It can be clearly seen that there is an obvious trough in the transverse hardness diagram, which is the Vickers hardness value measured around the pores. The poor microhardness indicates that the porosity has a great influence on the microhardness, due to the pores within the material collapsing under load[34].
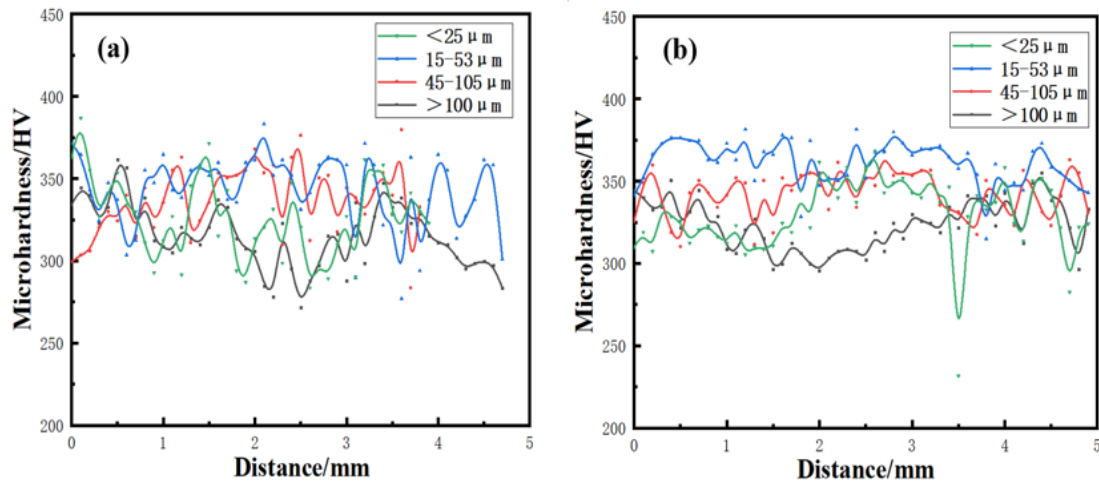
Fig. 16 Microhardness distribution chart of laser-additive RAFM with different particle size, (a) perpendicular to the scanning direction, (b) parallel to the scanning direction

Comparison of mechanical properties of different process experiments from literature[22, 35, 36] is tabulated in Table 4. We refer to the CLAM steel and RAFM steel produced by SLM, the CLAM steel rolled and the CLAM steel welded joints, and make a comparison with the RAFM steel manufactured in this experiment. It can be clearly seen that the tensile strength of SLM added CLAM steel and rolled CLAM steel is about 650 MPa. The tensile strength of RAFM steel manufactured by LMD process this time can reach 1057.75 MPa, which is much higher than that manufactured by other processes. Microscopic Vicker's hardness of various processes are similar, basically in 300-400 HV. In terms of Charpy impact energy, we chose a unified standard. It can be seen that except for the rolled CLAM steel, the Charpy impact energy manufactured by other processes is extremely low. We expect that the subsequent heat treatment process will improve its Charpy impact energy.

Table 4 Comparison of mechanical properties of different process experiments

Methods	Materials	Tensile Strength/MPa	Hardness/HV	Impact properties/J	Refs
As-welded joint	CLAM	650	---	>20	[35]
SLM	CLAM	650	400	10	[36]
SLM	RAFM	966.25	---	19.75	[22]

Rolling	CLAM	680	---	>200	[35]
LMD	RAFM (<25 μm)	926.77	330	8.15	This study
LMD	RAFM (15-53 μm)	1008.27	350	6.2	This study
LMD	RAFM (45-105 μm)	1057.75	347	7.45	This study
LMD	RAFM (>100 μm)	1029.14	310	15	This study

4. Conclusion

Laser Coaxial Powder Feeding Additive Manufacturing is a promising process for manufacturing RAFM steel. We can control the scanning path of the laser to achieve a complex component molding, avoiding the welding joint which has defect concentration. In this experiment, we not only explored LMD technology to manufacturing RAFM steel, but also compared the molding effect of additive with different powder size for the first time:

1. The RAFM steel manufactured in this experiment is well formed, without obvious surface defects, and has high density and good mechanical properties. The as-built microstructure consists of δ-ferrite, lath martensite and other precipitates. The tensile strength of RAFM prepared by LMD method can reach 1057.75MPa, which is much higher than that of rolled RAFM steel of 680 MPa, with an increase of about 55.56%. The hardness reaches 350HV and Charpy impact energy is 15J, which is close to that of SLM added RAFM steel.

2. We used high digital photography as the characterization method to monitor the changes of molten pool morphology during the coaxial powder feeding process. It is concluded that the molten pool is shorter and the solidification speed is faster in the laser additive process of coarse powder. This conclusion well explains the problem of large porosity in the sample manufactured by the coarse powder laser. The powder feeding gas brought into the molten pool by the powder particles has no time to escape due to the fast solidification rate, and is solidified in the as-built. The rapid solidification rate also leads to the smaller grain size and better mechanical properties of RAFM steel manufactured by coarse powder laser.

3. The tensile strength and toughness of RAFM steel increased with the increase of powder size. The hardness, tensile strength and toughness of RAFM steel with 45~105 μm powder size were the best among all powder size. Among them, a certain amount of pore appeared in RAFM steel with larger particle size, which results in a decrease in stress concentration and tensile strength.

4.   The surface of EBSD structure is typical columnar grain, which is fast solidification mechanism. The grain size is small, and there is no obvious microstructure orientation. Coarse powder has more spatter and lower utilization rate in manufacturing process.

RAFM steel with LMD additive has good surface forming morphology and excellent mechanical properties. The influence of powder particle size on laser additive process was explored by controlling the size of powder particle size. In the following research, laser addition of RAFM steel can be carried out by better powder parameter ratio, and other post-treatment processes can be used to obtain better RAFM steel.

References

1.   Klueh RL, Gelles DS, Jitsukawa S, et al (2002) Ferritic/martensitic steels - Overview of recent results. J Nucl Mater 307–311:455–465. https://doi.org/10.1016/S0022-3115(02)01082-6

2.   Dong SM, Katoh Y, Kohyama A, et al (2002) Microstructural evolution and mechanical performances of SiC/SiC composites by polymer impregnation/microwave pyrolysis (PIMP) process. Ceram Int 28:899–905. https://doi.org/10.1016/S0272-8842(02)00071-8

3.   Tavassoli AAF, Alamo A, Bedel L, et al (2004) Materials design data for reduced activation martensitic steel type EUROFER. J Nucl Mater 329–333:257–262. https://doi.org/10.1016/j.jnucmat.2004.04.020

4.   Zinkle SJ (2005) Advanced materials for fusion technology. Fusion Eng Des 74:31–40. https://doi.org/10.1016/j.fusengdes.2005.08.008

5.   Tanigawa H, Shiba K, Möslang A, et al (2011) Status and key issues of reduced activation ferritic/martensitic steels as the structural material for a DEMO blanket. J Nucl Mater 417:9–15. https://doi.org/10.1016/j.jnucmat.2011.05.023

6.   Tavassoli AAF (2002) Present limits and improvements of structural materials for fusion reactors - A review. J Nucl Mater 302:73–88. https://doi.org/10.1016/S0022-3115(02)00794-8

7.   Jitsukawa S, Tamura M, Van der Schaaf B, et al (2002) Development of an extensive database of mechanical and physical properties for reduced-activation martensitic steel F82H. J Nucl Mater 307–311:179–186. https://doi.org/10.1016/S0022-3115(02)01075-9

8.   Klueh RL, Nelson AT (2007) Ferritic/martensitic steels for next-generation reactors. J Nucl Mater 371:37–52. https://doi.org/10.1016/j.jnucmat.2007.05.005

9.   Wu Y (2006) Conceptual design activities of FDS series fusion power plants in China. Fusion Eng Des 81:2713–2718. https://doi.org/https://doi.org/10.1016/j.fusengdes.2006.07.068

10.   Wu Y (2008) Conceptual design of the China fusion power plant FDS-II. Fusion Eng Des 83:1683–1689. https://doi.org/https://doi.org/10.1016/j.fusengdes.2008.06.048

11.   Murdoch D, Glugla M, Hayashi T, et al (2008) Evolution of ITER Tritium Confinement strategy and adaptation to Cadarache site conditions and French regulatory requirements. Fusion Eng Des 83:1355–1358. https://doi.org/https://doi.org/10.1016/j.fusengdes.2008.04.006

12.   Wu Y (2007) Design analysis of the China dual-functional lithium lead (DFLL) test blanket module in ITER. Fusion Eng Des 82:1893–1903. https://doi.org/https://doi.org/10.1016/j.fusengdes.2007.08.012

13.   Li C, Huang Q, Zhang P (2007) Preliminary experimental study on Hot Isostatic Pressing diffusion bonding for CLAM/CLAM. Fusion Eng Des 82:2627–2633. https://doi.org/https://doi.org/10.1016/j.fusengdes.2007.04.021

14.   Eftink BP, Vega DA, El Atwani O, et al (2021) Tensile properties and microstructure of additively manufactured Grade 91 steel for nuclear applications. J Nucl Mater 544:152723. https://doi.org/10.1016/j.jnucmat.2020.152723

15.   Wu BD, Liu X, Li JF, et al (2021) Tungsten-chromium coatings on reduced activation ferritic/martensitic steels prepared by laser melting deposition process. J Nucl Mater 543:. https://doi.org/10.1016/j.jnucmat.2020.152573

16.   Olakanmi EO, Cochrane RF, Dalgarno KW (2015) A review on selective laser sintering/melting (SLS/SLM) of aluminium alloy powders: Processing, microstructure, and properties. Prog Mater Sci 74:401–477. https://doi.org/10.1016/j.pmatsci.2015.03.002

17.   Tradowsky U, White J, Ward RM, et al (2016) Selective laser melting of AlSi10Mg: Influence of post-processing on the microstructural and tensile properties development. Mater Des 105:212–222. https://doi.org/10.1016/j.matdes.2016.05.066

18.   Buchbinder D, Meiners W, Pirch N, et al (2015) components using selective laser melting Investigation on reducing distortion by preheating during manufacture of aluminum components using selective laser melting. 012004: https://doi.org/10.2351/1.4828755

19.   Zhang P, Zhang Q, Yan H, et al (2021) Fabrication, microstructure and micromechanical properties of Fe-based

metallic glass coating manufactured by laser. Surf Coatings Technol 405:.

https://doi.org/10.1016/j.surfcoat.2020.126726

20. Zhang P, Li M, Yan H, et al (2019) Microstructure evolution of Ni-Mo-Fe-Si quaternary metal silicide alloy

composite coatings by laser cladding on pure Ni. J Alloys Compd 785:984–1000.

https://doi.org/10.1016/j.jallcom.2019.01.191

21. Cheng Q, Shi H, Zhang P, et al (2020) Microstructure, oxidation resistance and mechanical properties of stellite

12 composite coating doped with submicron TiC/B4C by laser cladding. Surf Coatings Technol 395:125810.

https://doi.org/https://doi.org/10.1016/j.surfcoat.2020.125810

22. Huang B, Zhai Y, Liu S, Mao X (2018) Microstructure anisotropy and its effect on mechanical properties of

reduced activation ferritic/martensitic steel fabricated by selective laser melting. J Nucl Mater 500:33–41.

https://doi.org/https://doi.org/10.1016/j.jnucmat.2017.12.011

23. Huang B, Zhai Y, Liu S, Mao X (2018) Microstructure anisotropy and its effect on mechanical properties of

reduced activation ferritic/martensitic steel fabricated by selective laser melting. J Nucl Mater 500:33–41.

https://doi.org/https://doi.org/10.1016/j.jnucmat.2017.12.011

24. Spierings AB, Herres N, Levy G (2011) Influence of the particle size distribution on surface quality and

mechanical properties in AM steel parts. Rapid Prototyp J 17:195–202.

https://doi.org/10.1108/13552541111124770

25. Simchi A (2004) The role of particle size on the laser sintering of iron powder. Metall Mater Trans B Process

Metall Mater Process Sci 35:937–948. https://doi.org/10.1007/s11663-004-0088-3

26. Metz R, Machado C, Houabes M, et al (2007) Nitrogen spray atomization of molten tin metal: Powder

morphology characteristics. J Mater Process Technol 189:132–137.

https://doi.org/https://doi.org/10.1016/j.jmatprotec.2007.01.014

27. Zhu S, Guo Y, Ruan Q, et al (2020) Formation of adiabatic shear band within Ti-6Al-4V: An in-situ study with

high-speed photography and temperature measurement. Int J Mech Sci 171:105401.

https://doi.org/10.1016/j.ijmecsci.2019.105401

28. Zhou X, Liu Y, Yu L, et al (2015) Uniaxial diffusion bonding of CLAM/CLAM steels: Microstructure and

mechanical performance. J Nucl Mater 461:301–307. https://doi.org/10.1016/j.jnucmat.2015.03.033

29. Saeidi K, Gao X, Zhong Y, Shen ZJ (2015) Hardened austenite steel with columnar sub-grain structure formed

by laser melting. Mater Sci Eng A 625:221–229. https://doi.org/10.1016/j.msea.2014.12.018

30. Castle EG, Mullis AM, Cochrane RF (2014) Evidence for an extensive, undercooling-mediated transition in

growth orientation, and novel dendritic seaweed microstructures in Cu–8.9wt.% Ni. Acta Mater 66:378–387. https://doi.org/https://doi.org/10.1016/j.actamat.2013.11.027

31.   Huang Q (2014) Development status of CLAM steel for fusion application. J Nucl Mater 455:649–654. https://doi.org/10.1016/j.jnucmat.2014.08.055

32.   Zhang B, Dembinski L, Coddet C (2013) The study of the laser parameters and environment variables effect on mechanical properties of high compact parts elaborated by selective laser melting 316L powder. Mater Sci Eng A 584:21–31. https://doi.org/10.1016/j.msea.2013.06.055

33.   Zhong Y, Liu L, Wikman S, et al (2016) Intragranular cellular segregation network structure strengthening 316L stainless steel prepared by selective laser melting. J Nucl Mater 470:170–178. https://doi.org/10.1016/j.jnucmat.2015.12.034

34.   Wang D, Song C, Yang Y, Bai Y (2016) Investigation of crystal growth mechanism during selective laser melting and mechanical property characterization of 316L stainless steel parts. Mater Des 100:291–299. https://doi.org/10.1016/j.matdes.2016.03.111

35.   Liu S, Huang Q, Peng L, et al (2012) Microstructure and its influence on mechanical properties of CLAM steel. Fusion Eng Des 87:1628–1632. https://doi.org/10.1016/j.fusengdes.2012.06.008

36.   Zhai Y, Huang B, Mao X, Zheng M (2019) Effect of hot isostatic pressing on microstructure and mechanical properties of CLAM steel produced by selective laser melting. J Nucl Mater 515:111–121. https://doi.org/10.1016/j.jnucmat.2018.12.028